Lab on a Chip

Dynamic Article Links

Cite this: *Lab Chip*, 2011, **11**, 3838

www.rsc.org/loc

PAPER

1-Million droplet array with wide-field fluorescence imaging for digital PCR†

Andrew C. Hatch,[a] Jeffrey S. Fisher,[a] Armando R. Tovar,[a] Albert T. Hsieh,[a] Robert Lin,[a] Stephen L. Pentoney,[b] David L. Yang[b] and Abraham P. Lee*[a]

Received 27th June 2011, Accepted 25th August 2011
DOI: 10.1039/c1lc20561g

Digital droplet reactors are useful as chemical and biological containers to discretize reagents into picolitre or nanolitre volumes for analysis of single cells, organisms, or molecules. However, most DNA based assays require processing of samples on the order of tens of microlitres and contain as few as one to as many as millions of fragments to be detected. Presented in this work is a droplet microfluidic platform and fluorescence imaging setup designed to better meet the needs of the high-throughput and high-dynamic-range by integrating multiple high-throughput droplet processing schemes on the chip. The design is capable of generating over 1-million, monodisperse, 50 picolitre droplets in 2–7 minutes that then self-assemble into high density 3-dimensional sphere packing configurations in a large viewing chamber for visualization and analysis. This device then undergoes on-chip polymerase chain reaction (PCR) amplification and fluorescence detection to digitally quantify the sample's nucleic acid contents. Wide-field fluorescence images are captured using a low cost 21-megapixel digital camera and macro-lens with an 8–12 cm^2 field-of-view at 1× to 0.85× magnification, respectively. We demonstrate both end-point and real-time imaging ability to perform on-chip quantitative digital PCR analysis of the entire droplet array. Compared to previous work, this highly integrated design yields a 100-fold increase in the number of on-chip digitized reactors with simultaneous fluorescence imaging for digital PCR based assays.

Introduction

Lab on a chip devices continuously strive to provide more information and function in ever smaller packages. This becomes evident when considering the growth of on-chip microarrays and micro/nanoreactors for massively parallel or high-throughput processing.[1–4] On-chip nanowells and droplet reactors have gained attention in the field of digital biology for applications like single-cell analysis[5–7] and single-copy nucleic acid detection including: digital quantification of DNA,[8–17] monoclonal template amplification for bead-based gene sequencing,[18–20] reverse transcriptase (RT-PCR) for detection of single RNA fragments,[21,22] and multiplexed digital PCR.[16,23] Digital PCR platforms benefit from each reactor having its own microenvironment where the amplification in one reactor does not interfere with that of another. This provides a digital output of nucleic acid concentrations with increased quantitative resolution.[24] Furthermore, single DNA molecules can be quantified even in the presence of competing template sequences, which would otherwise skew traditional qPCR results.[25–27]

Unfortunately, the dynamic-range of on-chip digital PCR lags behind its analog counterparts by three to four orders of magnitude due to the lack of compartmentalized reactors and limited volume throughput.[8–14,21] This is further compounded by Poisson distribution behavior of single molecule encapsulation, which requires low concentrations of DNA relative to reactor number.[9,12,28] In addition, many nucleic acid processing schemes benefit from real-time fluorescence measurements, which provide temporal information about PCR amplification, but few high-throughput platforms provide this ability.[11,15,21,23,29–32] In this work, we aim to increase real-time imaging throughput as much as possible using techniques that process greater droplet numbers and avoid serial processing. Previous work by the authors present a means to increase droplet array packing density and utilize 100% of the imaging area.[13] The technology helps increase reactor imaging throughput while reducing the total area.

Presented in this work is a more highly integrated design that provides real-time imaging and high-throughput processing of over 1-million droplets. This is accomplished by integrating rapid droplet generation, on-chip thermocycling, and wide-field fluorescence imaging on a single microfluidic platform. Droplet generation rates of 3–8 kHz frequencies are achieved using a 256 droplet-splitter design. The 256 channel outlets also favor high

---

[a] *Department of Biomedical Engineering, University of California-Irvine, 3120 Natural Sciences II, Irvine, CA, 92697, USA. E-mail: aplee@uci.edu; Fax: +1 949-824-1727; Tel: +1 949-824-9691*

[b] *Beckman Coulter, Inc., 250 S. Kraemer Blvd., Brea, CA, 92821, USA. E-mail: dlyang@beckman.com; Fax: +1 714-961-3971; Tel: +1 714-961-3112*

† Electronic supplementary information (ESI) available: 256 Droplet splitting generation, macro-lens aperture, wide-field real-time fluorescence imaging, image processing, and interference filter characterization. See DOI: 10.1039/c1lc20561g

water/oil (w/o) volume ratios and uniform filling of a large viewing chamber. Wide-field fluorescence imaging of an 8–12 cm^2 area is achieved using a 21-megapixel camera and 100 mm macro-lens with 1× to 0.85× magnification, respectively. The combined process enables digital PCR quantification of 1-million droplets consisting of a 50 μL PCR sample volume and DNA template numbers up to 100 000 copies. The combined processing scheme results in a 100-fold increase in digitized reactor number for real-time imaging, which simultaneously increases throughput and dynamic-range of digital PCR assays.[8–14,21]

Materials and methods

Microfluidic devices

Microfluidic devices were fabricated using glass slides and polydimethylsiloxane (PDMS) patterned using standard soft lithography processes as illustrated in Fig. 1A.[33,34] Single-height microfluidic master molds of 78–80 μm thick SU-8 structures were fabricated on 3″ silicon wafers in a clean-room facility. Sylgard-184 PDMS (Dow Corning) was cast on top of the SU-8 molds and a 1 mm thick glass slide cut to 2″ × 2″ was embedded inside the PDMS layer spaced 225 μm above the viewing chamber using 30 awg Kynar wire. The embedded glass served to reduce deformation of the microfluidic chamber and create a vapor barrier to reduce oil and PCR reagents from evaporating during PCR thermocycling.[13,35] The PDMS was then cured in a 60 °C oven for 4–6 hours, released from the mold, inlet and outlet holes were cored, then bonded to 1 mm thick 2″ × 3″ glass slides (Corning, USA) using air plasma treatment (Harrick Plasma, USA). Finally, the entire device was placed in a 120 °C oven overnight to return the material to its native hydrophobic state. Fig. 1B shows the mask design used to pattern the SU-8 molds. The design consists of oil and PCR sample inlets, a flow focusing droplet generator, 256 droplet-splitting channels, and a 27 mm × 40.5 mm droplet viewing chamber.

256 Droplet splitter. Droplet generation was achieved using a single PCR sample inlet and oil inlet feeding into a flow focusing droplet generator to form a large ~13 nL parent droplet. This droplet then split 8 times to form 256 daughter droplets as shown in Fig. 1C and Video S1†. High w/o volume ratios and stable droplet generation were achieved using heavy white mineral oil (Fisher Scientific) combined with the stabilizing surfactants 3% w/w Abil EM 90 (Degussa/Goldschmidt) and 0.1% w/w Triton X-100 (Sigma-Aldrich). The first parent channel was designed with a width of 240 μm followed by 8 bifurcation junctions at 45° angles, with $\sqrt{2}$ width reductions between junctions 2 and 7, resulting in a final width of 30 μm at the outlet. Droplet generation was typically performed at flow rates of 8 μL min^{-1} PCR solution and 4 μL min^{-1} oil resulting in droplet generation frequencies of 2.66 kHz and 66% water/oil (w/o) volume ratios. Faster flow rates up to 25 μL min^{-1} PCR solution and 25 μL min^{-1} oil were also achieved resulting in a droplet generation frequency of 8.33 kHz and a 50% w/o volume ratio. Based on previous work published by the authors, w/o volume ratios ranging between 50% and 66% are favorable for various high-density single or double-layer droplet array packing configurations.[13]

PCR reagents. Taqman PCR solutions were prepared using a standard protocol of Amplitaq Gold Fast PCR Master Mix, UP (2×) PCR kit (Applied Biosystems). Proprietary sequences of template chlamydia DNA (150–300 bp), forward/reverse primer

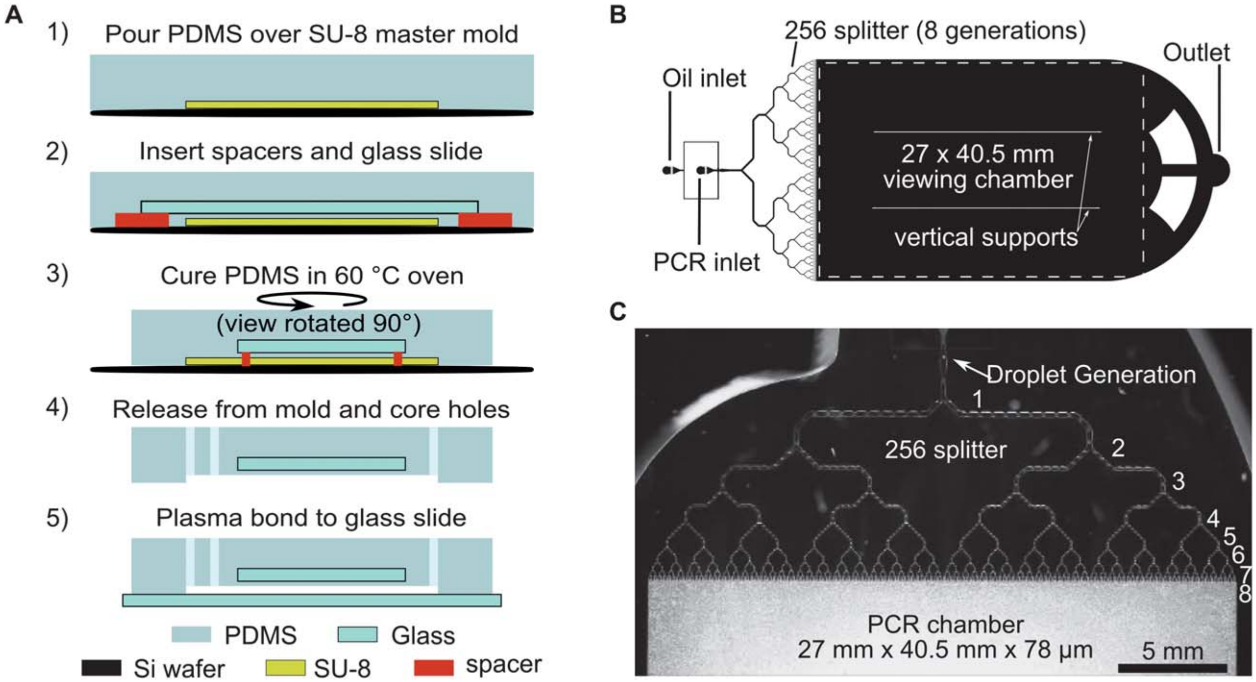

Fig. 1 Schematic illustration and images of the PCR microdevice: (A) fabrication process, (B) mask design of the droplet array with sample inlets, droplet generator, 256 splitter, viewing chamber and outlet. (C) The picture of droplet generation and 256 splitter filling the 27 mm × 40.5 mm viewing chamber.

pairs (15–20 nt), and FAM labeled probes (20–25 nt) were supplied by Beckman Coulter Inc. (USA) and ordered in high purity from Advanced Biotechnologies Inc. Solutions were prepared as 50 μL reactions with the following final concentrations: forward/reverse primers (0.9 μM), probe (0.3 μM), 1× PCR master mix, and DNA template dilutions ranging from 20–100 000 copies per reaction. BSA (1 μg μL^{-1}) was added to the solution to reduce surface adsorption of DNA or enzymes to surfaces and further stabilize the emulsion and PCR.[36–38] Other surface treatments/additives may also be used to reduce surface adsorption and stabilize the assay.[27,38–41]

Droplet array chamber. In order to increase reactor number and throughput as much as possible, a combination of factors were taken into consideration including droplet size, imaging area, and imaging resolution. Ultimately, a low cost imaging solution was selected that consisted of a consumer grade 21-megapixel digital camera. Based on this camera's sensor, a PCR assay of approximately 1 million droplets was chosen to provide a minimum resolution of no less than 15–20 pixels per droplet. For high throughput volume processing we chose a large 50 μL PCR reaction discretized into 1 million 50 pL droplets with 46 μm diameters. The minimum chamber area that could contain 1-million 46 μm spheres for visualization was theoretically determined to range from 18.3 cm^2 for traditional single layer close-packed droplets to only 6.1 cm^2 using a three-layer cubic close packed scheme.[13] For purposes of droplet visibility and optimal usage of the imaging area, a double layer (100) lattice like droplet packing configuration was chosen. This formation yields on average 945 drops mm^{-2}, requiring a total imaging area of ∼10.58 cm^2, an optimal chamber height of ∼78 μm, and a w/o volume ratio of ∼61.5%.[13]

With these parameters in mind, a chamber area of ∼11 cm^2 was designed with 27 mm × 40.5 mm dimensions following the 2 : 3 aspect ratio of the camera's imaging sensor. Two strips of vertical support structures were designed into the droplet chamber to prevent collapse during plasma bonding and to help maintain a more uniform height throughout the device during filling and thermocycling. This design provided a remaining chamber area of ∼10.7 cm^2 with an ∼83.7 μL volume capacity. Depending on the actual w/o volume ratio, chamber height, droplet size, and droplet packing arrangements, an estimated $1.03 \times 10^6 \pm 0.1 \times 10^6$ total droplets were expected to reside in the holding chamber. For accuracy, the total area processed during image analysis was adjusted to approximate a 1-million droplet region or 50 μL sample volume.

Wide-field fluorescence imaging

To view the ∼11 cm^2 area in a single snapshot, both a large field of view optical setup and a high-resolution imaging setup were required to adequately resolve all 1-million droplets. As illustrated in Fig. 2, large field of view images were captured using a Canon 5D Mark II digital single lens reflex (dSLR) camera with a 21 megapixel CMOS sensor and a 100 mm f/2.8 USM Macro Lens (Canon Inc., USA). The dSLR camera and lens were mounted to a photocopy stage and positioned 6–8 inches above a thermocycling setup with the microfluidic device on top. Fluorescence imaging ability was added using an Omniprint-1000 350W portable light source with a 3 mm fiber-optic cable (Omnichrome, USA), and a commercial GFP-3035 Brightline® filter set (Semrock, USA) with 25 mm excitation and 32 mm emission filters. A fiber optic wand with focusing objective and excitation filter was placed 5–8 inches above the device, at a 30-45° angle, to illuminate an area 1 cm wider than the chamber's longest diagonal or ∼5 to 6 cm. The 32 mm emission filter was positioned on the front of the lens.

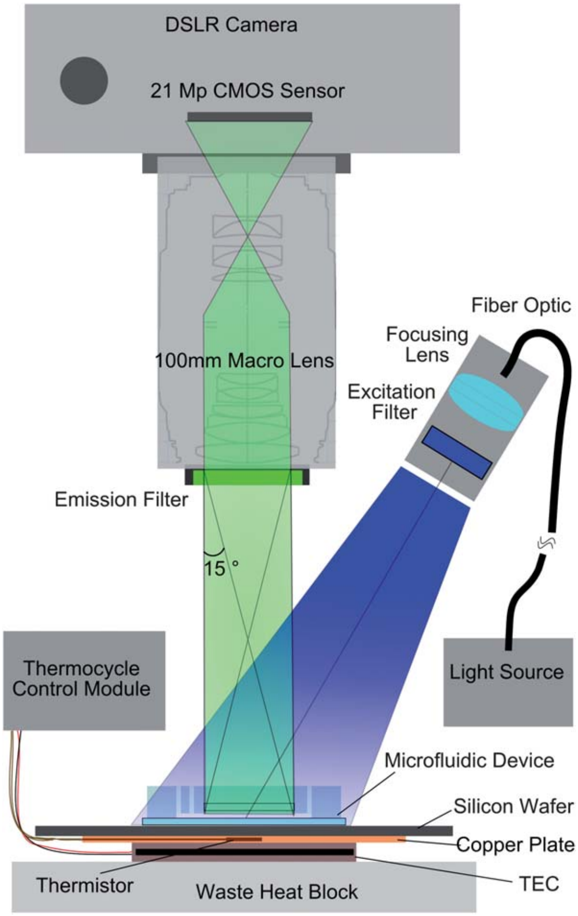

Fig. 2 Wide field of view fluorescence imaging setup.

The macro-fluorescence imaging setup is capable of imaging 8.6–17.2 cm^2 areas at 1× to 0.5× magnification, respectively. The Canon 5D Mark II sensor contains a 36 mm × 24 mm 3 : 2 format 3 color RGB CMOS sensor in an RGBG Bayer mosaic filter pattern with 6.4 μm pixel pitch and individual microlenses per pixel providing greater quantum efficiency. Image capture settings were typically taken at *f*/2.8 aperture, ISO‡ 400–800, 0.85× magnification, ∼6.5″ working distance, and 4–8 s exposure in RAW image format with long exposure noise reduction enabled. The 100 mm macro-lens provides a 6″ working focal distance from the front of the lens to the imaging plane and a focal depth of >100 μm at *f*-number, *f*/2.8 and 1× magnification. At this focal length, the camera has an equivalent numerical

---

‡ ISO represents the "International Organization for Standardization" and is a measure of sensitivity of the camera sensor to light. The higher the ISO the greater the gain of the signal for the same amount of light absorbed by the sensor.

aperture, NA, of ~0.089 as detailed in the ESI†.[42] Uniformity measurements of the fluorescence imaging system are detailed in the ESI† to show the behavior of the lens, fluorescence filters, and excitation light source. With these imaging parameters, 20–40 pixels per droplet resolution could be achieved for the 1-million droplet array.

On chip PCR thermocycling

Thermocycling of the microfluidic device was achieved using a 39.7 mm × 39.7 mm thermoelectric cooler (TEC) and a FTC-100 controller (Ferrotec Inc., USA) controlled using manufacturer software. Temperature feedback control was accomplished by inserting a 1 mm thick 2″ × 2″ copper plate between the microfluidic device and TEC unit with an embedded TR-1(2245) thermistor (Ferrotec Inc., USA). A custom-fabricated liquid-cooled aluminium block was placed beneath the TEC device to dissipate waste heat. Finally, a 3″ silicon wafer was placed between the copper plate and microfluidic device to help equalize heat distribution and provide a better optical surface for imaging as shown in Fig. 2. Two-step PCR thermocycling was initiated with a 10 minute "hot start" at 95 °C to activate the Taq-polymerase then 40–45 cycles of ramping between 58 °C and 95 °C using 30 second hold times and 2–3 $°C\ s^{-1}$ thermal ramp rates. The total PCR thermocycling reaction time required ~65 minutes. The ability to perform on-chip thermocycling of droplets was necessary to be able to perform real-time observation of the entire droplet reactor array during PCR amplification.

Digital PCR quantification and image processing

ImageJ software and custom Matlab code were used to systematically detect and quantify fluorescent droplets and analyze their size, packing geometry, density, and fluorescence intensity using methods similar to that presented in previous work.[13] Background subtractions, contrast enhancement, and flatfield corrections were performed as needed for quantification of digital PCR results. A first level background correction was performed using the camera's built-in peripheral illumination correction and long-exposure time noise correction. For digital PCR quantification, Fast Fourier Transfer (FFT) filtering was employed to quickly filter out unwanted spatial frequencies in intensity. This allowed a simple thresholding or local maxima detection scheme to quantify the digital PCR results. Positive droplets were detected using a maximum entropy or Otsu's method thresholding,[43] then their intensity could be measured from the original image. FFT analysis was also used to determine droplet lattice orientation and average droplet size, see ESI† for more information. The quantification results were then compared to the expected number of positive droplets for serial dilutions ranging from 20–100 000 copies per reaction.

Results and discussion

Wide-field fluorescence imaging

Bright field and fluorescence imaging of the droplet devices were performed directly in place to visualize droplet generation, chamber filling, and digital PCR amplification in real-time while PCR thermocycling was taking place. The fluorescence image in Fig. 3 shows ~1 million 50 picolitre drops in a 78–80 μm tall, 11 cm^2 viewing area. The droplets in these devices were sufficiently stable to undergo 40 or more cycles of on-chip thermocycling with less than 5% coalescence. Real-time fluorescence imaging of PCR amplification is demonstrated in Fig. 4 showing cycles 15–40 displayed in 5 cycle increments. These images were captured at 1× magnification using a smaller 4.5 cm^2 × 50 μm tall device with droplets arranged in a single layer hexagonal packing configuration. See Videos S2 and S3† of the real-time PCR amplification observed between cycles 15 and 44 captured once every cycle. Fig. S8† shows a plot of real-time fluorescence intensity *vs.* cycle number.

Due to all droplets containing only a single copy number, the absolute PCR efficiency of the assay could not be readily determined using standard calibration curves.[44,45] It is possible to use other methods for calculating PCR efficiencies based on intensity changes alone but these were difficult to implement due to the noise in cycle to cycle fluorescence intensity.[46,47] However, the digital nature of the PCR assay does enable a comparison between amplification curves that can be used for qualitative/semi-quantitative evaluation of amplification efficiencies within droplets. An example where this would be useful is measuring amplification efficiency across the entire device to determine thermocycling uniformity. Other advantages gained from real-time imaging include more sensitive detection of positively amplified droplets due to better background subtraction schemes, monitoring crosstalk of DNA among droplets, detecting droplet coalescence, tracking droplets, optimizing PCR cycle times, and others.

As common with any optical imaging system, sensitivity, uniformity, and resolution must be balanced against field-of-view, depth-of-focus, and cost. The techniques employed in this paper have overcome wide-field of view fluorescence imaging challenges in two ways. First, by packing the droplets in higher density, the illumination area is greatly reduced. This results in brighter excitation intensity and consequently, stronger fluorescence signals from the PCR amplified droplets. Likewise, using 3D droplet packing allows higher pixel/droplet resolution because the droplet overlap and 100% sensor area coverage allow more efficient usage of the sensor.[13] Second, the 1× magnification values and longer working distances provide greater depth of focus to view the 3D droplet lattices. This also reduces working angles of the optics to provide more even illumination and image capture of large areas by allowing the use of higher contrast interference filters. A more detailed discussion of the influence of incidence angles on the interference filters used in this imaging setup is provided in the ESI†.

The 21-megapixel CMOS sensor in the dSLR camera has a very high resolution and is relatively inexpensive, making it a useful off-the-shelf camera setup for capturing a large field of view. With this high resolution, a 20–40 pixels per droplet ratio could be achieved for a 1-million droplet array. Further increases in droplet number will require even greater pixel numbers to maintain a sufficient 15–20 pixels per droplet ratio required to resolve each independent droplet's fluorescence signal. This limit is determined based on the need to adequately resolve and detect round droplets for fluorescence imaging, accommodate droplet misalignment with the pixel grid, and compensate for the color filters on the sensor.

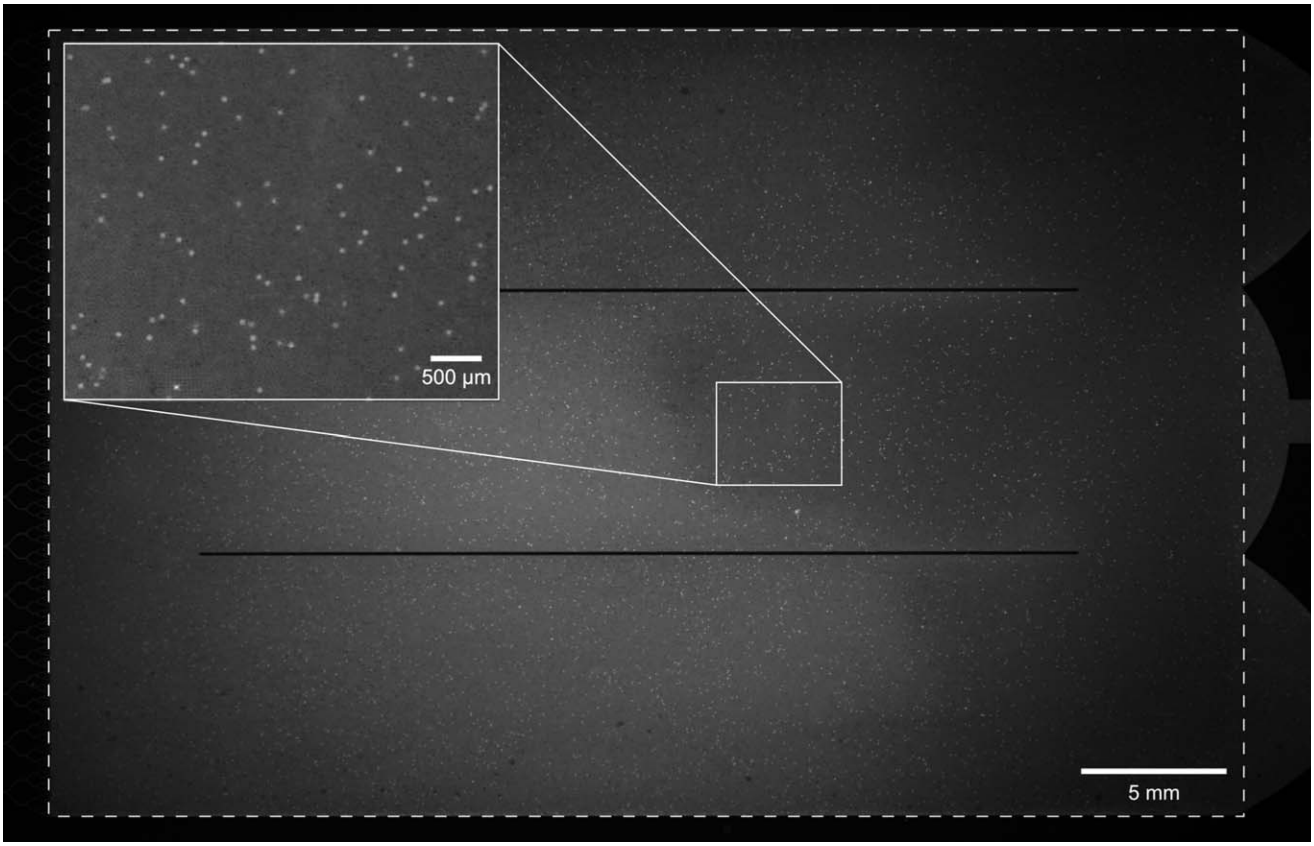

Fig. 3 Macro-fluorescence image of 1-million PCR amplified droplets in a 27 mm by 40.5 mm by 78–80 µm droplet chamber (highlighted by dashed white line) imaged on a 21-megapixel dSLR camera. The inset is an enlarged section for enhanced visualization.

Although cooled CCD sensors have been historically chosen over their CMOS counterparts due to less noise and higher signal gains, recent improvements in CMOS technology[48] have favored their growth and appearance in research for bioassays[49] and fluorescence detection.[50,51] For example, due to the camera's CMOS sensor having small 6.4 µm pixels with individual RGBG Bayer color filters, it is more prone to noise and requires a larger number of pixels for signal averaging. This has been improved by the incorporation of convex microlenses on each pixel to increase the quantum efficiency and sensitivity of the sensor. Furthermore, improved image processing schemes and CMOS readout techniques have helped to further reduce noise in the final digitized output. Some newly developed functions of modern dSLR cameras that we were able to utilize include: long-exposure noise-reduction, peripheral illumination correction, and high ISO gains with less noise. Similar improvements have been observed in the quality and variety of dSLR lenses. Overall the combination of a large field of view and low cost fluorescence imaging setup required for this application was beneficial, compensating for the losses in sensitivity and image quality compared to typical fluorescence microscopes.

Droplet generation and 256 splitter

Using the 256 droplet splitter design we were able to achieve rapid droplet generation at rates as high as 8.33 kHz with flow rates of 25 µL min^{-1} PCR solution and 25 µL min^{-1} oil flow rates creating 1-million droplets in just two minutes. In order to achieve higher w/o volume ratios for purposes of 3D droplet packing and to reduce satellite droplet formation in the splitting

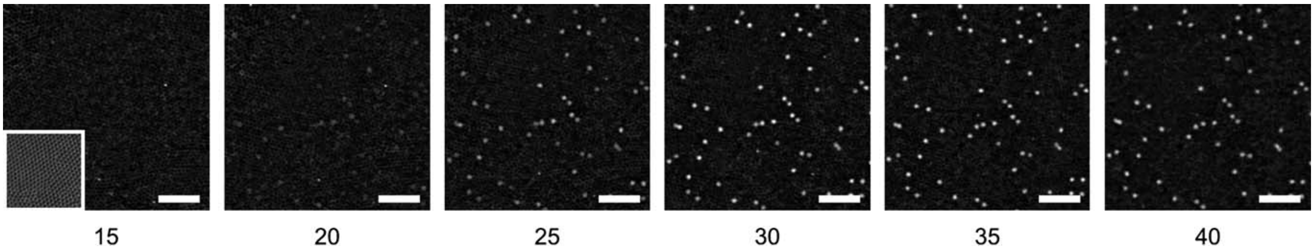

Fig. 4 Real-time imaging of PCR amplification between cycles 15–40. The small lower-left inset shows a bright field image of the droplet array before thermocycling began (scale bars 500 µm).

regions, generation was typically limited to 2–3 kHz production rates with consistent droplet uniformity and CV values of less than 8% (n = 500 000). At these rates, generation of 1-million droplets and filling of the chamber area could be achieved in less than 7 minutes. For multi-junction droplet splitting, interfacial tension and shearing rates are important, not only for droplet stability during droplet generation, but also for stabilizing the emulsion when packed into high density arrays. Reducing the interfacial tension too low resulted in poor parent droplet shearing rates and excessive satellite droplet formation. Alternatively, high interfacial tension in the droplets prevented them from splitting through all 8 channel bifurcations and made them prone to coalescence during thermocycling. For these experiments, the use of 0.1% Triton X-100 and 3% Abil EM 90 provided both a stable droplet emulsion and sufficient compatibility with the PCR assay.

Droplet packing and thermocycling

While exiting the 256 droplet splitter, droplets flowed evenly into the large viewing chamber as seen in the ESI, Video S1†. The even flow profile out of the 256 splitter made filling of the chamber easier and would tend to force out air bubbles that may have been trapped in the device during the initial sample filling stage. In earlier experiments, air bubbles remained behind in the chamber and caused problems during PCR thermocycling, as they would expand and contract dramatically and act as nucleation sites for sample evaporation. Ensuring tubing was free of bubbles and pre-filling the device with surfactant free oil helped to greatly reduce this problem to less than 5% failure rates in experiments.

Controlling droplet size, w/o volume ratio, and chamber height enabled predictive 3D droplet self-assembly into square packing (100) lattice orientations.[13] However, due to the deformability of droplets and PDMS, combined with variations in SU-8 mold height and actual droplet size, coexistence of both (100) square packing and (111) hexagonal packing formations would frequently occur. This is largely due to the nature of 3D droplet self-assembly requiring very small changes in height to switch between the (100) and (111) lattice configurations. In addition, w/o volume ratios were typically higher than optimal conditions which would cause droplets to deform and pack closer together. These possible sources of error in determining droplet number for digital PCR quantification were compensated for by measuring the actual droplet size and density from the image. The image area analyzed was then adjusted to accurately reflect 1-million droplets or a 50 µL sample with less than 8% error. Future modifications to reduce these problems would be to reduce channel heights to ~75 µm and decrease w/o volume ratios to prevent (111) lattice formations.

Digital PCR quantification

Digital quantification of the PCR amplified droplets seen in Fig. 3 was calculated and found to have a positive droplet fluorescence count of ~7450 that closely matched the expected value of 1 in ~133 positive droplets and a total of 7500 expected with less than 5% error. This device was estimated to contain ~1 100 000 droplets in the chamber based on calculations from a chamber volume of ~83 µL, droplet size of 46 µm, and PCR/oil volume ratio of 66.6%. The total PCR volume processed was ~55 µL of solution. Further analysis of corresponding bright field images showed average droplet sizes and packing densities with a total droplet count in good agreement with the theoretical volume based estimation having less than 5% error. Sensitivity of the system to detect and quantify droplets relied on fluorescence signal to noise levels, DNA concentration, and degree of droplet overlap.

The minimum threshold required to detect droplets was based on thresholding schemes that maximize the entropy of the histogram. Using real-time analysis actually helps to improve detection sensitivity because it allows a reference frame to subtract background noise compared to a single end-point frame. The temporal information also helps to differentiate between amplified signal and noise because the rate at which the intensity changes can be expected to follow a gradual increase from frame to frame, allowing another parameter by which to detect positive droplets. An example would include the change in intensity due to a piece of auto-fluorescent debris, or shrinking/evaporation of a droplet, resulting in a more concentrated solution over time. However, lattice shifting and droplet motion from frame to frame posed problems with the implementation of this scheme. Future work to fix the droplet lattice would prove advantageous.

A series of serial PCR dilutions from 20 to 100 000 copies per reaction were performed for 50 µL sample volumes and their total DNA content quantified and plotted in Fig. 5. As seen in the graph, even with the slight variations in droplet size or number from run to run, the total DNA concentrations closely match the predicted outcomes with average errors of less than 15% (N = 10). Considering well performed qPCR experiments can estimate original DNA concentrations to just fewer than

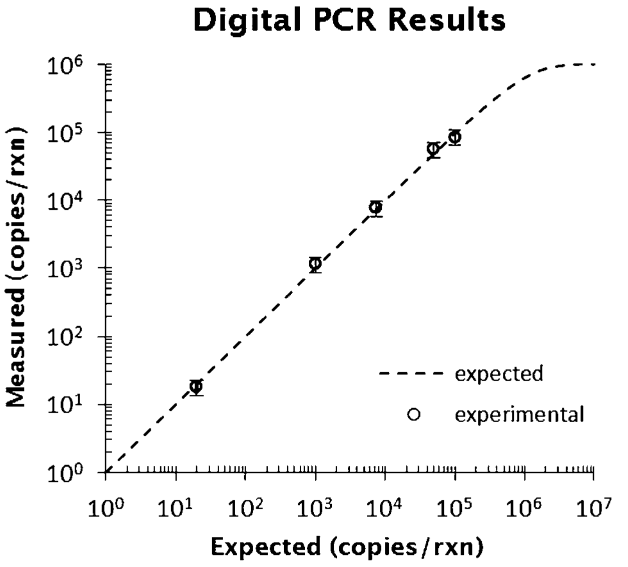

Fig. 5 Digital PCR experimental results of 1-million droplet arrays containing digital PCR dilutions at concentrations ranging from 2×10^1 to 1×10^5 copies per 50 µL reaction. Fluorescence images from the 21-megapixel digital camera were processed to quantify the total copy number present per 50 µL volume reaction. Relative standard error 15%.

1 cycle number variation, providing 150–200% error in original concentration estimations,[52,53] this is still a more than advantageous level of performance for digital PCR.[24] Furthermore, the resulting quantification errors are still comparable with the amount of error one would predict from Poisson distribution probabilities, 5–10% variation. For DNA concentrations lower than 10 copies per reaction, Poisson distribution probabilities predict that quantification errors would exceed 10% due to lack of statistically relevant events.

As long as the total PCR volume analyzed is relatively constant, and the DNA template concentration is relatively low compared to droplet number, with less than 1 in 10 positive droplets, very little quantification error would be expected even with moderate changes in droplet size or number. Based on this performance, an advantageous digital PCR quantification can be achieved over the range of 10–100 000 copies for 1-million droplets without the need for real time qPCR amplification curves or Poisson distribution corrections. This results in a reliable DNA detection sensitivity of 10-copies/50-μL rxn, with a possible detection sensitivity as low as 1–3 copies/50-μL rxn. Compared to other works on digital PCR, this system of 1-million droplets yields a 100-fold increase in non-serial digital PCR reactor number, and is the first to integrate a 1-million droplet array throughput with real-time imaging ability on a single microfluidic device.[8–14,21]

Image quantification required on average 0.5–1.5 hours depending on several factors including droplet lattice uniformity, fluorescence intensity uniformity, degree of droplet overlap and the percentage of the total droplets that were amplified. Single layer droplet arrays with low positive numbers required much simpler image processing techniques due to low levels of overlap. Non-uniform droplet lattices and high copy numbers required more complex image processing and lengthened analysis times. Real-time imaging analysis was especially time consuming due to the added number of image frames and the need to track droplets from frame to frame.

On average, an entire PCR sample could be completed in 2–4 hours with the longest steps being thermocycling at 1–1.5 hours and image processing at 0.5–1.5 hours. Improving these two processes would further improve the speed and efficiency of the high-throughput design. A future design to improve droplet lattice uniformity and reduce image processing complexity could be to pattern high and low spots in the chamber area for droplets to settle into, resulting in more uniform and fixed droplet arrays. Thermocycling efficiency could be reduced to 30 minutes or less by reducing the hot start time and using a more efficient thermocycling process such as a rapid air thermocycler.[11,54]

Conclusions

We have presented a useful approach to significantly increase the dynamic-range, throughput, and imaging ability of droplet arrays for on-chip digital PCR applications. This was achieved in a high throughput manner by integrating rapid droplet generation, thermocycling, and wide-field fluorescence imaging of 1-million droplets on a single microfluidic device. Our design enables both end-point and real-time analysis of droplets in an 8–12 cm^2 area during active PCR thermocycling. We demonstrate a 100-fold increase in reactor number over previous digital PCR arrays and maintain confidence levels of 15% for quantifiable results. The time saving benefits of this approach and novel integration of a variety of techniques to overcome small number/volume microfluidics should prove useful for the digital biology community.

Acknowledgements

This work was supported in part by the Defense Advanced Research Projects Agency (DARPA) N/MEMS S&T Fundamentals Program under grant no. N66001-1-4003 issued by the Space and Naval Warfare Systems Center Pacific (SPAWAR) to the Micro/nano Fluidics Fundamentals Focus (MF3) Center. Authors also thank Beckman Coulter Inc. for providing critical reagents and expertise relating to the work.

Notes and references

1 V. Taly, B. T. Kelly and A. D. Griffiths, *ChemBioChem*, 2007, **8**, 263–272.
2 A. D. Griffiths and D. S. Tawfik, *Trends Biotechnol.*, 2006, **24**, 395–402.
3 A. Huebner, S. Sharma, M. Srisa-Art, F. Hollfelder, J. B. Edel and A. J. deMello, *Lab Chip*, 2008, **8**, 1244–1254.
4 E. Brouzes, M. Medkova, N. Savenelli, D. Marran, M. Twardowski, J. B. Hutchison, J. M. Rothberg, D. R. Link, N. Perrimon and M. L. Samuels, *Proc. Natl. Acad. Sci. U. S. A.*, 2009, **106**, 14195–14200.
5 J.-C. Baret, V. Taly, M. Ryckelynck, C. A. Merten and A. D. Griffiths, *Med. Sci. (Paris)*, 2009, **25**, 627–632.
6 J. Clausell-Tormos, D. Lieber, J.-C. Baret, A. El-Harrak, O. J. Miller, L. Frenz, J. Blouwolff, K. J. Humphry, S. Koster, H. Duan, C. Holtze, D. A. Weitz, A. D. Griffiths and C. A. Merten, *Chem. Biol.*, 2008, **15**, 427–437.
7 Y. Schaerli and F. Hollfelder, *Mol. BioSyst.*, 2009, **5**, 1392–1404.
8 F. Shen, W. Du, J. E. Kreutz, A. Fok and R. F. Ismagilov, *Lab Chip*, 2010, **10**, 2666–2672.
9 M. M. Kiss, L. Ortoleva-Donnelly, N. R. Beer, J. Warner, C. G. Bailey, B. W. Colston, J. M. Rothberg, D. R. Link and J. H. Leamon, *Anal. Chem.*, 2008, **80**, 8975–8981.
10 E. A. Ottesen, J. W. Hong, S. R. Quake and J. R. Leadbetter, *Science*, 2006, **314**, 1464–1467.
11 S. O. Sundberg, C. T. Wittwer, C. Gao and B. K. Gale, *Anal. Chem.*, 2010, **82**, 1546–1550.
12 B. Vogelstein and K. W. Kinzler, *Proc. Natl. Acad. Sci. U. S. A.*, 1999, **96**, 9236–9241.
13 A. C. Hatch, J. S. Fisher, S. L. Pentoney, D. L. Yang and A. P. Lee, *Lab Chip*, 2011, **11**, 2509.
14 R. A. White, P. C. Blainey, H. C. Fan and S. R. Quake, *BMC Genomics*, 2009, **10**, 116.
15 N. R. Beer, B. J. Hindson, E. K. Wheeler, S. B. Hall, K. A. Rose, I. M. Kennedy and B. W. Colston, *Anal. Chem.*, 2007, **79**, 8471–8475.
16 Q. Zhong, S. Bhattacharya, S. Kotsopoulos, J. Olson, V. Taly, A. D. Griffiths, D. R. Link and J. W. Larson, *Lab Chip*, 2011, **11**, 2167–2174.
17 Y. Schaerli, R. C. Wootton, T. Robinson, V. Stein, C. Dunsby, M. A. Neil, P. M. French, A. J. Demello, C. Abell and F. Hollfelder, *Anal. Chem.*, 2009, **81**, 302–306.
18 Y. Zeng, R. Novak, J. Shuga, M. T. Smith and R. A. Mathies, *Anal. Chem.*, 2010, **82**, 3183–3190.
19 R. Gan, Y. Yamanaka, T. Kojima and H. Nakano, *Biotechnol. Prog.*, 2008, **24**, 1107–1114.
20 F. Diehl, M. Li, Y. He, K. W. Kinzler, B. Vogelstein and D. Dressman, *Nat. Methods*, 2006, **3**, 551–559.
21 N. R. Beer, E. K. Wheeler, L. Lee-Houghton, N. Watkins, S. Nasarabadi, N. Hebert, P. Leung, D. W. Arnold, C. G. Bailey and B. W. Colston, *Anal. Chem.*, 2008, **80**, 1854–1858.
22 M. Nakano, N. Nakai, H. Kurita, J. Komatsu, K. Takashima, S. Katsura and A. Mizuno, *J. Biosci. Bioeng.*, 2005, **99**, 293–295.

23 Z. Hua, J. L. Rouse, A. E. Eckhardt, V. Srinivasan, V. K. Pamula, W. A. Schell, J. L. Benton, T. G. Mitchell and M. G. Pollack, *Anal. Chem.*, 2010, **82**, 2310–2316.

24 S. Weaver, S. Dube, A. Mir, J. Qin, G. Sun, R. Ramakrishnan, R. C. Jones and K. J. Livak, *Methods*, 2010, **50**, 271–276.

25 R. Williams, S. G. Peisajovich, O. J. Miller, S. Magdassi, D. S. Tawfik and A. D. Griffiths, *Nat. Methods*, 2006, **3**, 545–550.

26 M. Hori, H. Fukano and Y. Suzuki, *Biochem. Biophys. Res. Commun.*, 2007, **352**, 323–328.

27 S. Kennedy and N. Oswald, *PCR Troubleshooting and Optimization: The Essential Guide*, Caister Academic Press, Norfolk UK, 2011.

28 P. J. Sykes, S. H. Neoh, M. J. Brisco, E. Hughes, J. Condon and A. A. Morley, *BioTechniques*, 1992, **13**, 444–449.

29 H. Kim, S. Dixit, C. J. Green and G. W. Faris, *Opt. Express*, 2009, **17**, 218–227.

30 R. Sista, Z. Hua, P. Thwar, A. Sudarsan, V. Srinivasan, A. Eckhardt, M. Pollack and V. Pamula, *Lab Chip*, 2008, **8**, 2091–2104.

31 J. Logan, *Real-Time PCR: Current Technology and Applications*, Caister Academic Press, Norfolk UK, 2009.

32 C. T. Wittwer, M. G. Herrmann, A. A. Moss and R. P. Rasmussen, *BioTechniques*, 1997, **22**, 130–131, 134–138.

33 G. M. Whitesides, E. Ostuni, S. Takayama, X. Jiang and D. E. Ingber, *Annu. Rev. Biomed. Eng.*, 2001, **3**, 335–373.

34 Y. Xia and G. M. Whitesides, *Annu. Rev. Mater. Sci.*, 1998, **28**, 153–184.

35 F. Courtois, L. F. Olguin, G. Whyte, D. Bratton, W. T. S. Huck, C. Abell and F. Hollfelder, *ChemBioChem*, 2008, **9**, 439–446.

36 E. Ostuni, R. Kane, C. S. Chen, D. E. Ingber and G. M. Whitesides, *Langmuir*, 2000, **16**, 7811–7819.

37 S. Poussier, J.-J. Chéron, A. Couteau and J. Luisetti, *J. Microbiol. Methods*, 2002, **51**, 349–359.

38 F. Courtois, L. F. Olguin, G. Whyte, A. B. Theberge, W. T. S. Huck, F. Hollfelder and C. Abell, *Anal. Chem.*, 2009, **81**, 3008–3016.

39 C. J. Beverung, C. J. Radke and H. W. Blanch, *Biophys. Chem.*, 1999, **81**, 59–80.

40 L. S. Roach, H. Song and R. F. Ismagilov, *Anal. Chem.*, 2005, **77**, 785–796.

41 H. Horakova, I. Polakovicova, G. Shaik, J. Eitler, V. Bugajev, L. Draberova and P. Draber, *BMC Biotechnol.*, 2011, **11**, 41.

42 J. Greivenkamp, *Field Guide to Geometrical Optics*, SPIE Press, Bellingham Washington, 2004.

43 P. K. Sahoo, S. Soltani and A. K. C. Wong, *Comput. Vision Graphics Image Process.*, 1988, **41**, 233–260.

44 K. K.-Y. Lai, L. Cook, E. M. Krantz, L. Corey and K. R. Jerome, *Clin. Chem.*, 2005, **51**, 1132–1136.

45 T. B. Morrison, J. J. Weis and C. T. Wittwer, *BioTechniques*, 1998, **24**, 954–958, 960, 962.

46 S. Cikos and J. Koppel, *Anal. Biochem.*, 2009, **384**, 1–10.

47 G. J. Boggy and P. J. Woolf, *PLoS One*, 2010, **5**, e12355.

48 A. El Gamal and H. Eltoukhy, *IEEE Circuits Devices Mag.*, 2005, **21**, 6–20.

49 D. M. Vykoukal, G. P. Stone, P. R. C. Gascoyne, E. U. Alt and J. Vykoukal, *Angew. Chem., Int. Ed.*, 2009, **48**, 7649–7654.

50 L. Shen, M. Ratterman, D. Klotzkin and I. Papautsky, *Sens. Actuators, B*, 2011, **155**, 430–435.

51 J. M. Song, M. Culha, P. M. Kasili, G. D. Griffin and T. Vo-Dinh, *Biosens. Bioelectron.*, 2005, **20**, 2203–2209.

52 B. Zimmermann, W. Holzgreve, F. Wenzel and S. Hahn, *Clin. Chem.*, 2002, **48**, 362–363.

53 B. Bubner, K. Gase and I. Baldwin, *BMC Biotechnol.*, 2004, **4**, 14.

54 K. Chapin and T. L. Lauderdale, *J. Clin. Microbiol.*, 1997, **35**, 2157–2159.